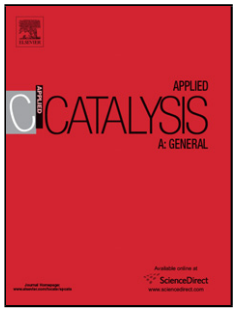

Title: Mn-based mixed oxides for low temperature NOx adsorber applications

Authors: Yaying Ji, Dongyan Xu, Mark Crocker, Joseph R. Theis, Christine Lambert, Agustin Bueno-Lopez, Deb Harris, Dave Scapens

PII: S0926-860X(18)30438-1
DOI: https://doi.org/10.1016/j.apcata.2018.09.006
Reference: APCATA 16806

To appear in: *Applied Catalysis A: General*

Received date: 11-7-2018
Revised date: 4-9-2018
Accepted date: 10-9-2018

Please cite this article as: Ji Y, Xu D, Crocker M, Theis JR, Lambert C, Bueno-Lopez A, Harris D, Scapens D, Mn-based mixed oxides for low temperature NOx adsorber applications, *Applied Catalysis A, General* (2018), https://doi.org/10.1016/j.apcata.2018.09.006

Mn-based mixed oxides for low temperature NOx adsorber applications

Yaying Ji[1], Dongyan Xu [1,2], Mark Crocker[1,3*], Joseph R. Theis[4*], Christine Lambert[4], Agustin Bueno-Lopez[5], Deb Harris[6], Dave Scapens[6]

[1]*Center for Applied Energy Research, University of Kentucky, Lexington, KY 40511, USA*

[2]*College of Chemical Engineering, Qingdao University of Science and Technology, Qingdao266042, PR China*

[3]*Department of Chemistry, University of Kentucky, KY 40506, USA*

[4]*Chemical Engineering Department, Ford Motor Company, 2101 Village Road, Dearborn, MI 48121, USA*

[5]*Department of Inorganic Chemistry, University of Alicante, Ap. 99, 03080 Alicante, Spain*

[6]*MEL Chemicals, Manchester M27 8LS, United Kingdom*

*Corresponding author: e-mail: mark.crocker@uky.edu; Tel.: +1 (859) 257-0295; Fax: +1 (859) 257-0302

Graphical abstract

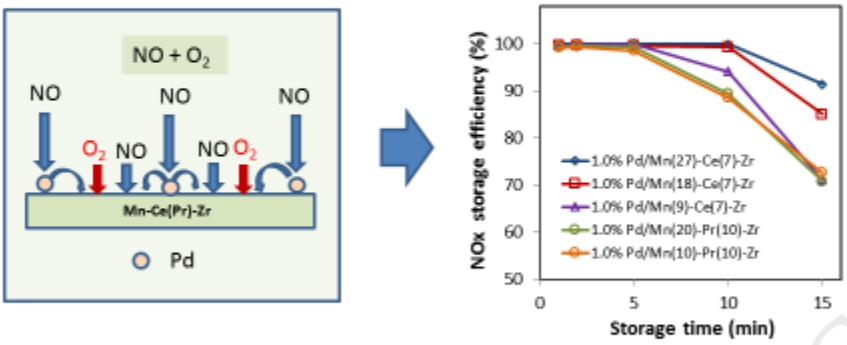

Highlights

- Pd-promoted Mn-Ce-Zr and Mn-Pr-Zr mixed oxides showed remarkably high NOx storage efficiency in the range 80 – 160 °C
- NOx storage efficiency in isothermal storage experiments was found to improve with increasing Mn content for 1%Pd/Mn-Ce-Zr materials
- DRIFTS measurements showed that relative to Ce-Zr mixed oxides, Mn incorporation favored NOx storage as nitrate
- NOx stored on Pd/Mn-Ce(Pr)-Zr mixed oxides desorbed at lower temperatures than for Ce-Zr mixed oxides

Abstract

Pd-promoted ternary oxides of the type Mn-Ce-Zr and Mn-Pr-Zr were characterized and evaluated for low temperature NOx storage applications such as diesel vehicle cold starts. While X-ray diffraction data were in all cases consistent with the formation of solid solutions, Mn/Zr and Mn/Ce(Pr) ratios found by XPS were consistently higher than the bulk values, indicative of an enrichment of Mn at the surface of the solids. Both sets of Pd-promoted mixed oxides showed

remarkably high NOx storage efficiency in the range 80 – 160 °C, while a 1.8% Pd/Mn(27)-Ce(7)-Zr catalyst showed excellent NOx storage in simulated cold start experiments. Moreover, ramping the temperature to 370 °C in these experiments, simulating higher speed operation, resulted in near complete purging of stored NOx from the catalyst. NOx storage efficiency in isothermal storage experiments was found to improve with increasing Mn content for the 1%Pd/Mn(x)-Ce(7)-Zr series (x = 9, 18, 27 wt.%), DRIFTS measurements showing that relative to Ce-Zr mixed oxides, Mn incorporation favored NOx storage as nitrate. During temperature programmed desorption (TPD) two main desorption events were observed, corresponding to decomposition of nitrites (up to 200 °C), followed by loss of nitrates (□200 - 400 °C). Nitrates stored on Pd/Mn-Ce(Pr)-Zr mixed oxides desorbed during TPD at lower temperatures than for CeO_2-ZrO_2 mixed oxides, a finding attributed to the lower basicity of Mn compared to Ce. Hydrothermal aging of 1.8%Pd/Mn(27)-Ce(7)-Zr at 700 °C reduced NOx storage efficiency, although the catalyst was still able to store significant amounts of NOx. However, catalyst sulfation led to a large decrease in NOx storage efficiency and the efficiency could not be completely recovered with lean or rich desulfations at high temperatures.

Keywords: manganese; cerium; palladium; NOx adsorption; low temperature

1. Introduction

The development of more efficient internal combustion engines represents a key enabler for decreasing CO_2 emissions and reducing the consumption of petroleum. However, the lower exhaust temperatures which result from improvements to engine efficiency represent a challenge for the control of pollutant emissions. Standard aftertreatment technologies such as three-way

catalysts (TWCs), diesel oxidation catalysts (DOCs) and selective catalytic reduction (SCR) fail to function efficiently at low temperatures, from which it follows that high efficiency internal combustion engines require new and/or improved technologies which specifically address this issue [1,2]. This is made imperative by the implementation of Tier 3 legislation, which will require that both NOx and hydrocarbons (HC) are effectively controlled during cold starts. Moreover, implementation of new combustion technologies under development will also require aftertreatment systems which can function effectively at the low exhaust temperatures which typify their normal operation.

One potential solution to this challenge employs a low temperature NOx adsorber (LTNA) device, also known as a passive NOx adsorber (PNA), in combination with a downstream NOx conversion catalyst. In this concept the upstream LTNA adsorbs NOx emitted from the engine during cold starts and then releases the NOx at higher temperatures, i.e., temperatures which are sufficiently elevated for the downstream TWC or SCR catalyst to efficiently convert the NOx [1-6]. Ideally, NOx is stored directly as NO, without requiring an NO oxidation step. Moreover, if a hydrocarbon trap and oxidation function is incorporated in the LTNA catalyst, the potential exists to mitigate both NOx and HC cold start emissions [7,8].

While various materials have been studied for LTNA applications, two main classes can be identified in the form of ceria-based mixed oxides [5,6,9-13] and Pd-exchanged zeolites [8,14-17]. Workers at Johnson Matthey [5,6] were the first to claim the use of CeO_2 as a LTNA component, promoted with either Pt or Pd. Recently, our group investigated Pt- and Pd-promoted CeO_2 and Ce-Zr mixed oxides for LTNA applications [9-11], demonstrating that Pt and Pd show different promotional behavior with respect to NOx adsorption and desorption. Theis [12] reported that compared to Pt-promoted Ce-Zr and Pt/Pd-promoted Al_2O_3, Pd-promoted Ce-Zr

mixed oxides provided the best combination of NO storage in the presence of C_2H_4 and H_2O above 100 °C and near complete NO_x release at the maximum bed temperature (□400 °C). Other advantages included low NO_2 and N_2O formation and cost effectiveness. Similarly, Kim and co-workers [13] found Pd/CeO_2 to be an effective material for low temperature NOx storage (80-160 °C) and thermally induced NOx release.

In this context, it is noteworthy that Mn-based mixed oxides have been widely investigated for NO oxidation and selective catalytic reduction (SCR). Wang et al. investigated Mn-mullite, (Sm, Gd)Mn_2O_5, for NO oxidation [18] and found that materials of this type can show even better NO oxidation performance than current commercial Pt-based catalysts. Qi and Li reported the use of Mn-Ce mixed oxides for NO oxidation [19] and noted that the high NO oxidation activity of this material was improved by incorporation of ZrO_2 into MnO_x-CeO_2. Due to its high activity for NO oxidation activity, Mn has been found to be an effective additive for Ba-based lean NOx trap (LNT) catalysts, improving lean phase NOx storage efficiency [20-22].

Mn-based mixed oxides have also attracted interest for low temperature NOx adsorption. Huang and Yang investigated a series of Fe-Mn-based ternary oxides for NO adsorption at 25 ºC [23]. These mixed oxides achieved efficient reversible NO adsorption, with Fe-Mn-Ti showing the best performance (45 mg/g NOx capacity) compared to Fe-Mn oxides doped with Zr, Ce, Ni, Co and Cu. Mn-Ce binary oxides were studied for NOx adsorption at 150 ºC by Machida et al. [24,25], excellent NOx uptake being observed at temperatures lower than 150 ºC. Li et al. [26] studied NO adsorption on MnOx catalysts and found that a catalyst containing a single α-Mn_2O_3 phase displayed the best NO adsorption, NO being mainly adsorbed in the form of NO/nitrites and NO_2/nitrates at low and high temperatures, respectively. Recently, Li and co-workers [27] reported a study of lean phase NOx storage and rich phase release over Mn_2O_3, Mn_3O_4 and

MnO_2 model catalysts at low temperatures (≤ 200 °C). NOx trapping ability was strongly linked to NO oxidation activity, the presence of Mn^{3+} ions and surface active oxygen species being implicated as important for high NO oxidation activity.

Given the potential of Mn-based oxides for low temperature NO adsorption, in this work the effect of doping Mn into Ce-Zr and Pr-Zr mixed oxides was examined, the resulting mixed oxides being promoted with Pd. Ternary Mn-Pr-Zr oxides have been little studied, however, like Ce^{4+}, Pr^{4+} is readily reduced to the +3 oxidation state with the creation of lattice vacancies that can facilitate NOx storage [10]. Microreactor studies were performed to characterize the NOx sorptive behavior of the materials during simulated cold starts, including the effect of added CO and C_2H_4 on NOx adsorption, and in situ DRIFTS measurements were used to characterize the surface species formed during NO adsorption and their subsequent thermal evolution.

2. Experimental

2.1. Catalyst preparation

Two series of Mn-based ternary mixed oxides were employed in this study, which are hereafter denoted as Mn(x)-Ce(y)-Zr and Mn(x)-Pr(y)-Zr (x and y representing the mole percentages of Mn and Ce or Pr in the mixed oxide, respectively). These materials were provided by MEL Chemicals and prepared by a proprietary aqueous precipitation process. Pd-promoted mixed oxides were prepared by incipient wetness impregnation (IWI) using an aqueous solution of tetraammine palladium nitrate to give a Pd loading of 1.0 wt.%, followed by drying at 50 ºC in a vacuum oven overnight to avoid water-mediated Pd precursor migration prior to calcination at 500 ºC for 3 h. Further, Mn(27)-Ce(7)-Zr was also promoted with 1.8 wt.% Pd using the same procedure, the resulting powder being washcoated onto cordierite monolith cores (400 cpsi, 6.5

mil, 3/4″(D) × 1.5″(L)) with a target washcoat loading of 200 g/L. It should be noted that characterization of this catalyst was performed using the powder (i.e., prior to washcoating).

2.2. Catalyst characterization

BET surface area and pore volume measurements were performed by nitrogen adsorption at -196 ºC using a Micromeritics Tri-Star 3000 system. Catalyst samples were outgassed overnight at 160 ºC under vacuum prior to the measurements. X-ray powder diffraction was conducted on a Phillips X'Pert diffractometer using Cu-Kα radiation (λ = 1.540598 Å). Diffractograms were recorded between 5º and 90º (2Θ) with a step of 0.02°. X-ray photoelectron spectroscopy (XPS) analysis was performed using a K-Alpha spectrophotometer (ThermoScientific) with a high-resolution monochromator. The binding energy was adjusted using the C 1s transition, appearing at 284.6 eV. Measured binding energy values were accurate to ±0.2 eV. Temperature-programmed reduction (TPR) was performed using Micromeritics AutoChem II Analyzer. Ca. 150 mg of catalyst was loaded in the reactor and pretreated in 10% O_2/N_2 at 500 °C for 1 h. After cooling the sample to room temperature (RT), TPR was carried out in a 10% H_2/Ar flow with a ramp of 10 °C/min from RT to 500 °C. The H_2 signal during TPR was monitored using a TCD.

CO pulsed chemisorption was performed to determine the average Pd particle size using a Micromeritics AutoChem II Analyzer. Around 200 mg of the catalyst was loaded into the reactor. After being reduced at 300 ºC in 10% H_2/Ar for 30 min, the catalyst was heated to 400 ºC (hold time 10 min) in flowing Ar to remove adsorbed H. Pulsed CO chemisorption was initiated using a four-way valve after the catalyst had been cooled to 0 ºC. During this measurement, 0.5 ml of CO was pulsed into the reactor every 2 min, the CO signal at the reactor outlet being monitored with a thermal conductivity detector (TCD). CO pulsing was terminated

after the TCD signal had reached a constant value, i.e., the precious metal sites were saturated with CO. Assuming a 1:1 ratio of CO to surface Pd, the overall metal dispersion was calculated based on the amount of CO adsorbed.

2.3. NOx adsorption and desorption

NO_x storage and desorption efficiencies of the powder catalysts were determined in a quartz microreactor equipped with a Pfeiffer Thermostar GSD301 mass spectrometer as described elsewhere [11]. Samples (175 mg) were equilibrated under a flow of 3.5% H_2O, 5.0% CO_2 and 5% O_2 (bal. He, 120 sccm) at the designated storage temperature, after which NO_x storage was initiated by adding 300 ppm NO to the feed. In all cases, a total flow rate of 120 sccm was used, corresponding to an approximate gas hourly space velocity (GHSV) of 30,000 h^{-1}. At the completion of the storage period (15 min), the feed gas was switched to bypass mode and the NO flow was switched off. When the NO concentration had dropped to zero, the gas was re-directed to the reactor and temperature programmed desorption (TPD) was carried out using a ramp rate at 10 °C/min from the storage temperature up to 500 °C. NO_x storage efficiency (NSE) is defined as the percentage of NO_x passed over the catalyst that is stored, while NO_x desorption efficiency (NDE) is defined as the percentage of stored NO_x desorbed during TPD, i.e.:

$$NSE = \left[1 - \frac{\int_0^{t_{ads}} F_{out}\, dt}{\int_0^{t_{ads}} F_{in}\, dt}\right] * 100\ (\%)$$

$$NDE = \left[\frac{\int_{t_{T_0}}^{t_T} F_{out}\, dt}{NSE * t_{ads} * F_{in}}\right] * 100\ (\%)$$

where t_{ads} is the NO_x storage time; F_{in} is the inlet NO_x mole fraction; F_{out} is the outlet NO_x mole fraction during either NO_x storage or the subsequent NO_x desorption period; t(To) is the start

time of NO_x-TPD corresponding to the NO_x storage temperature before the temperature is raised; t(T) is the end time of NO_x-TPD corresponding to the desired NO_x desorption temperature.

Hydrothermal aging of the powder catalysts was performed at 750 ^oC for 16 h under feed gas containing 5% CO_2, 3.5% H_2O and 5% O_2 (balance He, GHSV = 30,000 h^{-1}).

For the monolithic catalysts, simulated cold start experiments were performed on a transient bench reactor where the catalyst was exposed to a subset of the temperatures encountered by the diesel oxidation catalyst (DOC) on the Ford Super Duty diesel truck during typical driving. To begin a test, the oven was cooled to 70 ^oC, and the feed gas was bypassed around the oven and stabilized with the desired gas composition. For all tests, the feed gas contained 110 ppm NO, 5% CO_2, 5% H_2O, 10% O_2, and N_2 for the balance. On some tests, the mixture also contained 250 ppm C_2H_4, 1300 ppm CO + 430 ppm H_2, or both C_2H_4 and CO/H_2 at these concentrations to assess the effects of these reductants on the NOx storage and release performance. The total flow rate remained constant at 6.4 L/min throughout the test, resulting in a space velocity of 30,000 h^{-1} for the 1″ by 1″ monolith samples.

Once the feed gas concentrations were stabilized, the exhaust was directed back through the reactor, and the oven began ramping immediately at 10 ^oC/min from 70 ^oC to 175 ^oC and held for 10 minutes. The oven was then ramped at 10 ^oC/min from 175 to 300 ^oC and held for 5. The NO and any reductants were then turned off, and the oven was cooled as quickly as possible to 70 ^oC for the next test. For an initial assessment of catalyst thermal durability, the sample was aged for 15 h at 700 ^oC with 10% O_2, 5% CO_2 and H_2O, and N_2 for the balance. This was followed by additional transient testing.

To assess sample sensitivity to sulfur poisoning, the sample was exposed to 5 ppm SO_2 at 350 ºC for 15 h with 10% O_2, 5% CO_2 and H_2O, and N_2 for the balance. The poisoned sample was then evaluated in transient tests. Lean desulfations were performed by turning off the SO_2 and exposing the poisoned sample to various temperatures ranging from 760 ºC to 815 ºC for ca. 15 min with 10% O_2, 5% CO_2 and H_2O, and N_2 for the balance, followed by additional transient tests. If the lean desulfations were insufficient to recover the NOx storage performance, the sample was desulfated under rich conditions for ca. 15 min with 3% CO + 1% H_2, 5% CO_2 and H_2O, and N_2 for the balance, followed by additional transient tests.

2.4. Diffuse Reflectance Infrared Fourier Transform Spectroscopy (DRIFTS)

DRIFTS measurements were performed using a Nicolet 6700 IR spectrometer equipped with a Harrick Praying Mantis accessory and MCT detector. The reaction cell was sealed with a dome equipped with two ZnSe windows and one SiO_2 observation window. The temperature of the reactor cell was controlled and monitored by a K-type thermocouple placed beneath the reaction chamber. For each DRIFT spectrum, an average of 115 scans was collected (requiring ca. 1 min) with a resolution of 4 cm^{-1}. The spectrometer as well as the outside of the reaction cell were continuously purged with dry nitrogen to avoid diffusion of air into the system. Unless otherwise stated, catalyst samples (~50 mg) were pretreated in situ in flowing 5% O_2/Ar (120 sccm) at 500 ºC for 1 h in order to remove moisture and carbonate, after which background spectra were collected (using the same feed gas) in the range 500 ºC to 100 ºC at intervals of 50 ºC. NOx storage was carried out at 100 ºC for 30 min using a feed consisting of 5% O_2 and 300 ppm NO (120 sccm). During NOx storage spectra were collected as a function of time. After 30 min of NOx storage, temperature programmed desorption (TPD) was performed in flowing 5% O_2/Ar

flow (120 sccm), the temperature being raised from 100 ºC to 500 ºC at a rate of 10 ºC/min. DRIFT spectra were recorded during TPD at intervals of 50 ºC. Absorbance spectra were obtained by subtracting background spectra from the spectra collected during NOx storage and desorption.

3. Results

3.1. Catalyst characterization

The physical properties of the materials are compared in Table 1. BET surface areas for the 1.0% Pd/Mn(x)-Ce(y)-Zr series ranged from 78-129 m^2/g. Higher Mn content tended to result in increased specific surface areas, although the correlation was not monotonic. This trend can be explained on the basis that as Mn content increased, so the Zr content of the samples decreased. XRD data demonstrated that a monoclinic ZrO_2 phase was present in low Mn-content (high Zr-content) samples (see below). With increased Mn content, a solid solution of Mn-Ce-Zr was formed, which exhibited increased surface area. Surface areas and pore volumes for the two 1.0% Pd/Mn(x)-Pr(y)-Zr mixed oxides were slightly higher than their Ce-containing counterparts, although it should be noted that the corresponding Mn and Ce/Pr contents for the two series were slightly different. Notably, hydrothermal aging caused a significant drop in BET surface area and pore volume of the 1.8% Pd/Mn(27)-Ce(7)-Zr sample, the specific surface area (SSA) decreasing from 100.5 to 20.7 m^2/g. Simultaneously, the average pore size increased, indicating that aging resulted in the collapse of pores. From the significant decline in SSA and pore volume it is evident that the Mn-doped Ce-Zr mixed oxide was less thermally stable than the undoped material [11].

From CO chemisorption measurements a Pd particle size of 6.7 nm was obtained for the 1% Pd promoted Mn(27)-Ce(7)-Zr sample, this increasing slightly to 8.2 nm upon increase of the Pd loading to 1.8%. Significant growth of the Pd particles was indicated for 1.8% Pd-promoted Mn(27)-Ce(7)-Zr after aging, the Pd sintering appearing to be more severe as compared to the Pd-promoted Ce-Zr system [11]. However, given the extensive pore collapse in the materials during aging, it is likely that the apparent growth of the Pd particles is a consequence of the entrainment of some fraction of the Pd particles in the support, these being inaccessible during CO chemisorption.

According to powder X-ray diffraction measurements, the Mn-Ce-Zr mixed oxides mainly exhibited tetragonal structure [11], as featured by two diffraction peaks at 30º (002) and ca. 35º (200) (Fig. 1a). For the samples with low Mn content, additional weak diffraction peaks were observed at ca. 28º and ca. 31º which are characteristic of the monoclinic ZrO_2 phase [11]. Evidently, increasing the level of Mn doping in the Ce-Zr-based mixed oxide stabilized the tetragonal structure. As compared to Mn-Ce-Zr mixed oxides, Mn-Pr-Zr oxides showed less intense bands at 30º and ca. 35º, consistent with a lower degree of crystallization of the tetragonal structure. Moreover, increasing the Mn content in Mn-Pr-Zr weakened the crystallization of the tetragonal phase, as evidenced by further decrease in the intensity of the band at 30º. Simultaneously, the observation of broad bands close to the peak at 30º suggested a partial phase change from tetragonal to monoclinic.

Fig. 1b compares the XRD patterns of the washcoat powder Mn(27)-Ce(7)-Zr promoted with 1.8% Pd before and after aging. A tetragonal phase was maintained after aging, however, significant crystallite growth was observed, as evidenced by an increase in the mean crystal size from 7.79 to 17.14 nm. Moreover, additional peaks at ca. 32º, 33º and 36º were observed after

aging, these being characteristic of Mn_3O_4 (JCPDS No. 24-0734) and Mn_2O_3 (JCPDS No. 41-1442) [26]. This suggests that some degree of segregation of the Mn phase occurred during aging. It is also noteworthy that no Pd diffraction features were observed for the aged samples, although sintering of the Pd particles was indicated by pulsed CO chemisorption. This is consistent with the idea that Pd particles underwent encapsulation in the support during aging.

H_2-TPR profiles of 1.8% Pd-promoted Mn(27)-Ce(7)-Zr before and after aging are depicted in Fig. 2. For comparison purposes, 1% Pd-promoted Mn(27)-Ce(7)-Zr is also included. The latter sample exhibited one main reduction peak at ca. 90 ^oC, implying that Pd and surface Mn/Ce reduction must occur simultaneously via H spillover from Pd. In addition, very weak H_2 uptake was observed in the range 300-600 °C, which by inference is related to the reduction of either bulk Mn ions or surface Mn/Ce ions located far from Pd. In comparison, for unpromoted Ce-Mn mixed oxides a series of reduction peaks are observed in the range 180 - 470 °C which have been assigned to sequential reduction of Mn^{4+} ions as well as surface Ce^{4+} ions [19,28]. For H_2-TPR of Mn-Zr mixed oxides, similar broad reduction peaks are observed in the range 250 - 550 °C for Mn ions [29]. Increasing the Pd loading to 1.8% resulted in the appearance of an additional peak at ca. 110 ^oC, suggesting the presence of two different types of Pd. Aging caused these two reduction peaks to shift to higher temperature, indicative of a stronger interaction between Pd and the Mn(27)-Ce(7)-Zr support, albeit the change in Pd particle size can also impact the Pd reduction feature.

XPS spectra for the samples, corresponding to the Mn 2p energy region, are shown in Figs. S1-S2. Deconvolution of the spectra indicates the presence of Mn in multiple oxidation states. As described elsewhere [30,31], a correlation should exist between formal Mn oxidation state and the energy difference between the main Mn 3s signal and the satellite peak. Indeed, an excellent

correlation was obtained for MnO, Mn_3O_4, Mn_2O_3 and MnO_2 reference samples (Fig. S3), from which the average oxidation of Mn in the samples can be calculated. As shown in Table S1, average oxidation states ranged from 3.1 to 3.7, with the exception of 1% Pd/Mn(27)-Ce(7)-Zr, for which an oxidation state of 2.1 was calculated. The lower oxidation state in this case is likely related to the high Mn content of the sample and the resulting tendency of Mn phase segregation to occur (see below). Pd $3d_{5/2}$ binding energies were also analyzed and found to span the range 337.2-338.0 eV for the samples. These values are characteristics of Pd in the +2 oxidation state, consistent with the presence of Pd(II) ions. However, reported Pd $3d_{5/2}$ binding energies for PdO span a wide range, at least 335.9-337.2 eV [32], such that the presence of PdO in the samples is also possible.

Surface Mn/Ce(Pr), Mn/Zr and Ce(Pr)/Zr atomic ratios for the samples, determined by XPS, are summarized in Table S2, which also shows the corresponding bulk atomic ratios. For the fresh samples the surface and bulk Ce/Zr ratios show good agreement, consistent with the presence of a solid solution, while the Pr/Zr ratios are indicative of slight surface enrichment by Pr. Notably, the surface Mn/Zr and Mn/Ce(Pr) ratios are consistently higher than those of the bulk, indicating there is an enrichment of Mn at the surface of the samples. This finding is consistent with a previous study of sol-gel CeO_2-ZrO_2-MnO_x mixed oxides, in which it was found that only a small fraction of Mn cations were incorporated into the CeO_2-ZrO_2 lattice to form solid solutions, the remainder existing on the surface as finely dispersed Mn_3O_4 [33]. Despite this, the doping was found to result in strong interactions between manganese oxide and ceria, both in the bulk and on the surface. The ready substitution of Ce^{4+} by Mn^{3+} in the fluorite structure is well documented [19,24], however, it is evident that substitution of Mn^{3+} into ZrO_2 can result in phase segregation. Indeed, Gutiérrez-Ortiz et al. [29] observed that while incorporation of small

amounts of MnO_x (10 and 20 mol%) into ZrO_2 led to the formation of solid solutions with a cubic structure, higher MnO_x concentrations resulted in the formation of a separate, crystalline, α-Mn_2O_3 phase. In the present case, such a crystalline phase was not observed, indicating that MnO_x existing at the surface of the mixed oxides must be very highly dispersed in the as-prepared samples.

Raman measurements were also performed on the samples (see Figs. S4 and S5). All of the spectra contain a weak band at ca. 650 cm^{-1} that can be attributed to a separated Mn_3O_4 phase [28,34]. Consequently, the band became relatively more intense as increasing amounts of Mn were incorporated into CeO_2-ZrO_2 (Fig. S4), consistent with increased phase segregation and formation of Mn_3O_4. However, based on the absence of corresponding X-ray diffraction peaks, such a phase must be highly dispersed. For the Mn-Ce-Zr samples, XPS data exhibited a trend of decreasing average Mn oxidation state with increasing 650 cm^{-1} band intensity, consistent with a decrease in Mn oxidation upon segregation, although no such trend was observed for the 1%Pd/Mn(10)-Pr(10)-Zr and 1%Pd/Mn(20)-Pr(10)-Zr samples.

3.2. NOx storage and desorption behavior

NOx adsorption and desorption behavior was investigated for the 1.0%Pd/Mn(27)-Ce(7)-Zr sample. As shown in Fig. 3, regardless of the storage temperature, 100% NOx storage efficiency (NSE) was achieved for the first minute in each experiment. In the case of thermal NOx release, a clear trend between NOx desorption efficiency (NDE) (< 300 ^oC) and storage temperature was observed in which NDE ranked in the order 80 ^oC >120 ^oC >160 ^oC. However, almost no difference in NDE was observed when the desorption temperature reached 350 ^oC, nearly 70% NDE being achieved in all three cases. To understand the role of Pd addition, results for NO

adsorption on the bare material at 120 ^{o}C and subsequent desorption are included in Fig. 3. The bare material showed lower NSE, particularly after 5 min, as well as lower NDE (< 300 ^{o}C) than its Pd-promoted analogue. Clearly, the addition of Pd improved both NOx storage and desorption behavior.

To obtain insights into the impact of Mn doping, the 1% Pd-promoted Mn-Ce-Zr and Mn-Pr-Zr samples with various levels of Mn doping were evaluated at 120 ^{o}C. As shown in Fig. 4, NSE of 100% was achieved for the first two minutes regardless of catalyst formulation, although differences in NSE were observed at longer storage times. Increasing the Mn content in the 1.0% Pd/Mn-Ce-Zr materials resulted in higher NSE, such that after 15 min storage a NSE of 92% was achieved for 1.0% Pd/Mn(27)-Ce(7)-Zr compared to 73% NSE for 1.0% Pd/Mn(9)-Ce(7)-Zr oxide. This suggests that Mn functions as a major NOx storage component in Mn-Ce-Zr mixed oxides and/or oxidized NO to NO_2, which is stored more effectively than NO. However, almost no difference in NSE was observed between the two 1.0% Pd/Mn-Pr-Zr materials. Indeed, unlike 1.0% Pd/Mn-Ce-Zr, increasing the Mn content in 1% Pd/Mn-Pr-Zr from 10 mol% to 20 mol% made a negligible impact on NSE. However, a reference sample containing no Mn, namely 1% Pd/Pr(20)-Zr (see Fig. S6), showed only 32% NSE after 5 min as compared to almost 100% NSE for the 1%Pd/Mn-Pr-Zr samples, indicating that the presence of Mn is essential for efficient NOx storage.

Turning to NOx desorption, two NOx desorption events were observed during NOx-TPD over the 1%Pd/Mn-Ce-Zr series (Fig. 4b and 4c), one occurring below 200 ^{o}C and the other occurring between 200 and 400 ^{o}C. The high temperature desorption peak slightly shifted to a higher temperature with decreased Mn content. Likewise, the 1% Pd/Mn-Pr-Zr series also exhibited two NOx desorption events during NOx-TPD. However, both desorption peaks were shifted to higher

temperatures as compared to the 1%Pd/Mn-Ce-Zr series, and a further shift of the high temperature desorption peak to higher temperature with decreased Mn content was also observed for the 1%Pd/Mn-Pr-Zr series. The NDE profiles during TPD are compared in Fig. 4c. A clear effect of Mn content on NOx desorption below 200 °C is apparent, higher Mn contents delaying the release of NOx. Notably, NDE values generally failed to exceed 80%, suggesting that a portion of the stored NOx was associated with ZrO_2 sites. As noted elsewhere, nitrate species adsorbed on ZrO_2 exhibit high thermal stability [35].

The impact of hydrothermal aging at 750 °C for 16 h on NOx adsorption and desorption behavior was investigated for the 1.0% Pd-promoted Mn(27)-Ce(7)-Zr and Mn(10)-Pr(10)-Zr samples, as shown in Fig. 5a; for comparison, data for the fresh samples are included in the figure. Aging caused a significant decrease in NSE over the 1.0% Pd/Mn(27)-Ce(7)-Zr sample, evidenced by a fall in the 5 min NSE from 100% to 50%. Likewise, the 1.0% Pd/Mn(10)-Pr(10)-Zr sample exhibited a decline in NOx storage performance after aging, although 80% NSE was still achieved for the first 5 min of storage. From the NOx desorption efficiency plot depicted in Fig. 5b, it is evident that for 1.0% Pd/Mn(27)-Ce(7)-Zr aging shifted NOx release to lower temperatures but caused only a minor deterioration in NDE at 350 ^{o}C. In contrast, the aged 1.0%Pd/Mn(10)-Pr(10)-Zr sample showed little NOx release below 200 ^{o}C while NDE at 350 ^{o}C actually improved.

As depicted in Fig. 5c, similar to the fresh samples, two desorption events were observed after aging. However, in both cases the high temperature desorption peak shifted to a slightly lower temperature as compared to the fresh state. Moreover, aging caused a significant decrease in NOx release up to 350 ^{o}C for 1.0%Pd/Mn(27)-Ce(7)-Zr, whereas 1.0%Pd/Mn(10)-Pr(10)-Zr was

affected to a lesser degree (48.4 μmol deNOx/g released after aging *versus* 58.74 μmol deNOx/g before aging).

3.3. DRIFTS study

3.3.1 Pd-promoted Mn(27)-Ce(7)-Zr

DRIFTS measurements were conducted to identify the surface species formed during NOx storage and their evolution during subsequent NOx-TPD. Fig. 6 compares two sets of spectra collected during NOx storage at 100 ^{o}C over Pd-promoted Mn(27)-Ce(7)-Zr. For the 1% Pd-promoted sample, a bridging nitrate band at 1610 cm^{-1} was observed early on during storage at the cost of monodentate and/or polydentate carbonate species, evidenced by a negative band at ca. 1350 cm^{-1} [36]. Several additional bands gradually became noticeable, corresponding to chelating bidentate nitrate (1585 cm^{-1}), monodentate nitrate (1546 cm^{-1} and 1528 cm^{-1}) and monodentate nitrite (1453 cm^{-1} and 1422 cm^{-1}) [37,38]. Monodentate nitrite became the most significant species present on the surface after 20 min, consistent with our previous report that Pd promotion favors NOx storage as nitrite [8,9]. It is also noteworthy that relative to the nitrate bands present, the nitrite bands observed for Pd-Mn(27)-Ce(7)-Zr were less intense compared to $Pd/Ce_{0.2}Zr_{0.8}O_2$ (for spectra collected under identical conditions) [11], inferring that Mn incorporation improved the NO and/or nitrite oxidation activity of the Ce-Zr mixed oxide. Given the presence of multiple, overlapping IR bands in the spectra shown in Fig. 6, it was not possible to identify characteristic Mn-based NOx bands, a task that is further complicated by the sheer variety of bands and assignments that have been reported for NOx adsorbed on manganese oxides [27,39,40]. When the Pd loading was increased to 1.8% rather different spectra were

obtained (Fig. 6b). Specifically, the higher Pd loading favored NOx stored as monodentate nitrate rather than bidentate nitrate and monodentate nitrite species.

The evolution of surface species during NOx-TPD is depicted in Fig. 7. For the sample containing 1% Pd, bands due to monodentate nitrite became less intense with increasing temperature and disappeared by 300 ^{o}C. Simultaneously, a significant increase in nitrate band intensity was observed with increasing temperature, particularly for the monodentate nitrates (~1540 cm^{-1}). These nitrate bands reached their peak intensity at 350 ^{o}C, indicating that a significant amount of nitrite species converted to nitrate during NOx-TPD. At 500 ^{o}C, a fraction of the nitrate species still remained on the surface. For 1.8% Pd-promoted Mn-Ce-Zr, the nitrate bands remained largely unchanged up to 400 ^{o}C, after which the bands diminished in intensity albeit some nitrate species remained on the surface at 500 ^{o}C.

In order to probe the role of Pd, NOx storage and TPD was also performed using an unpromoted sample of Mn(27)-Ce(7)-Zr. Figures S7 and S8 show DRIFT spectra obtained during NOx storage at 100 °C on Mn(27)-Ce(7)-Zr, as well as their evolution during subsequent TPD. For comparison purposes, the corresponding spectra obtained for 1% Pd/Mn(27)-Ce(7)-Zr are included in the figures. Notably, nitrates (1625 – 1533 cm^{-1}) were the dominant species formed during NOx storage on bare Mn-Ce-Zr. In the case of the Pd-promoted sample, relatively more nitrite (~1450 cm^{-1}) was formed on the surface, demonstrating that Pd facilitated NOx storage as less stable nitrite. Moreover, during TPD little change was observed in the NOx bands up to 400 °C for the bare material, while the Pd-promoted material showed significant decomposition of nitrate/nitrite bands below 400 °C, indicating that NOx stored on the bare material is more stable than that observed on the Pd-promoted analogue.

3.3.2 Pd-promoted Mn(10)-Pr(10)-Zr

DRIFTS studies were also carried out over the Mn(10)-Pr(10)-Zr material promoted with 1.0% Pd. Similar to the 1.0% Pd/Mn(27)-Ce(7)-Zr sample, bridging nitrate was formed during the early stages of NO adsorption on 1.0% Pd/Mn(10)-Pr(10)-Zr (Fig. 8). Chelating and monodentate nitrate bands gradually formed and increased in intensity with time, monodentate nitrate giving rise to the most intense band after 20 min. Moreover, bands due to monodentate nitrite (1458 cm^{-1} and 1426 cm^{-1}), bidentate nitrite and/or ionic nitrate (1330-1300 cm^{-1}) and bidentate or chelating (1204 cm^{-1}) nitrite species grew in over time. During subsequent NOx-TPD, all of the nitrite bands disappeared by 300 ^{o}C. No significant differences in the evolution of the nitrate species were observed compared to 1.0% Pd/Mn(27)-Ce(7)-Zr. However, a significant amount of nitrate species remained on the surface at 500 ^{o}C compared to 1.0% Pd/Mn(27)-Ce(7)-Zr, which may reflect the higher Zr content of 1.0% Pd/Mn(10)-Pr(10)-Zr.

3.4 Evaluation of 1.8% Pd/Mn(27)-Ce(7)-Zr in simulated cold start experiments

Given the promising NOx storage and release behavior of 1.8% Pd/Mn(27)-Ce(7)-Zr, a fresh monolithic sample of it was prepared and evaluated on a transient bench reactor. After a mild degreening at 500 °C, the catalyst was evaluated in transient tests with no reductant present, with 250 ppm C_2H_4 added and with 1350 ppm CO + 450 ppm H_2 present in the feed. Figure 9 shows the NOx slip ($NO+NO_2$) emitted from the reactor during the initial 800 s of the tests with these different test conditions. Relative to the NOx slip on the test with no reductant, the NOx slip with 250 ppm C_2H_4 was slightly lower during the first 125 s of the test. However, the NOx slip with C_2H_4 was significantly higher between 250 and 570 s of the test and even exceeded the feed

gas level during that time. For the test with the CO/H_2 mixture, the NOx slip during the first 125 s was the highest of the three tests, and it was also higher between 250 and 480 s relative to the test with no reductant. Hence, neither C_2H_4 nor the CO/H_2 mixture was beneficial for the NOx storage performance of this formulation.

A key feature of passive NOx adsorbers is the ability to release all of the stored NOx during warmed-up operation. To assess the extent of NOx release on the preceding tests, the cumulative amounts of stored NOx over the approximately 2000 s tests are shown in Fig. 10. Ideally, the cumulative amount of stored NOx would return to zero by the end of the test. Consistent with Fig. 9, the maximum amount of NOx stored during the test was lower with C_2H_4 or CO/H_2 than with no reductant. This suggests that not only are the reductants not beneficial for the NOx storage performance, they actually interfere with the NOx storage performance of the catalyst. However, for each test condition, the cumulative amount of stored NOx returned to very low levels by the end of the test. This indicates that the catalyst was essentially purged of all the stored NOx in the presence or absence of reductant. This would allow the maximum NOx storage performance during a subsequent test.

The 1.8% Pd/Mn(27)-Ce(7)-Zr catalyst was aged for 15 h at 700 °C on the reactor with the lean mixture and evaluated on several transient tests with no reductant. Figure 11 compares the NOx slip on one test with the degreened sample and on two tests with the thermally aged sample. The aged sample slipped more NOx than the degreened sample, particularly during the initial 150 s of the tests. However, the thermally aged catalyst still demonstrated significant NOx storage capability.

The aged catalyst was then exposed to 5 ppm SO_2 under lean conditions at 350 °C for 15 h and evaluated for NOx storage performance with no reductants. Figure 12 shows that the NOx storage performance was severely degraded by the sulfur poisoning. Attempts were made to desulfate the catalyst by exposing it to approximately 15 minutes under lean conditions at 760 °C, 790 °C, and 815 °C. Figure 13 shows that the 760 °C desulfation had little impact on the NOx storage performance, but desulfations at 790 °C and 815 °C resulted in some partial recovery of the NOx storage performance. However, the performance was still relatively poor after the 815 °C desulfation. While not shown here, subsequent desulfations at 700 °C and 750 °C under rich conditions were also attempted on the same catalyst sample, but the NOx performance only worsened. At this point elemental analysis revealed the absence of sulfur in the sample (S < 0.1 wt.%), indicating that the inability to recover the NOx storage performance was due to thermal damage to the sample (sintering and phase segregation). It was concluded that sulfur poisoning is a major challenge for this Mn-containing formulation.

4. Discussion

For the samples prepared in this study, the Ce(Pr)/Zr ratios determined by XPS generally showed good agreement with the bulk values, consistent with the presence of a solid solution. In contrast, the Mn/Zr and Mn/Ce(Pr) ratios found by XPS were consistently higher than those of the bulk, indicative of an enrichment of Mn at the surface. For all of the samples, Raman spectra contained a weak band at ca. 650 cm^{-1} that can be attributed to a separated Mn_3O_4 phase, the band becoming more intense as increasing amounts of Mn were incorporated into CeO_2-ZrO_2. These findings are in line with previous reports suggesting that only very limited amounts of Mn can be incorporated into CeO_2-ZrO_2 and ZrO_2 lattices, segregation of Mn as a highly dispersed Mn_3O_4 [33] or α-Mn_2O_3 [29] phase occurring readily.

In the absence of sulfur, the Mn-Ce(Pr)-Zr mixed oxides showed excellent NOx storage efficiency at low temperatures, the Mn clearly playing a key role in NOx storage. From DRIFTS measurements it can be surmised that Mn incorporation improved oxidation of NO and/or nitrite to NO_2 and/or nitrate, in agreement with the literature for MnO_x-CeO_2 mixed oxides [19,24,41]. Moreover, NOx desorption from Pd/Mn-Ce(Pr)-Zr mixed oxides, as depicted in Fig. 4c, follows a pattern similar to that reported for MnO_x-CeO_2 [24]. In both cases a low temperature desorption peak is observed ($\leq$ 200 °C), together with a much larger peak at higher temperature (peak maximum at ca. 300 °C). Machida et al. [24] assigned the desorption events to respectively loss of bidentate/monodentate nitrates and ionic nitrate. In contrast, our DRIFTS-TPD measurements indicate that the main species desorbing from Pd/Mn-Ce(Pr)-Zr up to 200 °C correspond to nitrites, after which nitrates (monodentate, bidentate and bridging) are decomposed. This is broadly in line with our previous findings for Ce-Zr mixed oxides [11], albeit the presence of manganese clearly favors nitrate formation over nitrite as a result of its high oxidation activity that in turn limits the amount of NOx that desorbs below 200 °C. Assignment of the low temperature peak to nitrites is also consistent with the progressive increase in low temperature NOx desorption observed for 1.0%Pd/Mn(27)-Ce(7)-Zr upon lowering the NOx storage temperature (Fig. 3b); at lower storage temperatures decreased rates of oxidation should result in a relatively larger fraction of the stored NOx existing as nitrites.

Notably, nitrates formed on MnO_x-CeO_2 [24] and Pd/Mn-Ce(Pr)-Zr mixed oxides are desorbed during TPD at lower temperatures than for CeO_2-ZrO_2 mixed oxides; indeed, in our previous work nitrates stored on Pd/Ce-Zr were released in the temperature range 300-450 °C, with a maximum at 390 °C after NOx storage at 120 °C [11]. This can be rationalized on the basis that Mn is less basic compared to Ce, as exemplified by their different O1s binding energies (ca.

529.4 eV for MnO_x and 528.5 eV for CeO_2) [24]. Both thermodynamic calculations and reaction data have demonstrated that the basicity of the component is directly related to its NOx trapping performance by being directly related to the calculated reaction equilibrium constants for the trapping reaction [42]. Hence, it was observed that for both series of Pd/Mn-Ce-Zr and Pd/Mn-Pr-Zr mixed oxides, lowering the Mn loading resulted in a shift of the main NOx release peak towards higher temperatures. For automotive applications, NOx release at moderate temperatures is required to ensure adequate adsorber regeneration, e.g., 200 – 300 °C, and hence samples with reasonably high Mn content such as Pd/Mn(27)-Ce(7)-Zr would be preferred.

In the case of MnO_x-CeO_2 mixed oxides, NO adsorption is thought to proceed via reaction of NO with surface oxygen species weakly bound to Mn, forming NO_2 adsorbates [19,24,27], albeit the exact form of the oxygen is unclear. However, the results of several studies indicate that on MnO_x-CeO_2 oxygen species such as superoxide (O_2^-) and peroxide (O_2^{2-}) can form at anion vacancies [19,43,44], e.g.:

$$Ce^{3+}\text{-}\square\text{-}Mn^{(n-1)+} + O_2 \rightarrow Ce^{4+}\text{-}O_2^-\text{-}Mn^{(n-1)+} \quad (1)$$

$$Ce^{4+}\text{-}O_2^-\text{-}Mn^{(n-1)+} \rightarrow Ce^{4+}\text{-}O_2^{2-}\text{-}Mn^{n+} \quad (2)$$

Both superoxide and peroxide are thought to be intermediates in the dissociation of O_2, leading to the incorporation of O_2 into the lattice [19,28]. Given that such superoxide and peroxide species are known to be weakly bound and highly reactive, oxidation of NO is likely to proceed via reaction with the adsorbed O_2^- and O_2^{2-}. In the case of the Pd/Mn-Ce(Pr)-Zr samples, similar reactions could occur at other types of anion vacancies present, i.e., Pr^{3+}-□-$Mn^{(n-1)+}$ and $Mn^{(n-1)+}$-□- Zr^{4+}. Once formed, NO_2 adsorption would occur at adjacent ion pairs (Mn^{n+}-O^{2-}, Ce^{4+}-O^{2-}) to

form nitrate species. As for other metal oxide sorbents [9-13], Pd acts as a promoter for these Mn-containing mixed oxides. Specifically, Pd can adsorb NO, which can spill over onto the oxide surface with subsequent formation of nitrite and/or nitrate. Comparison of DRIFT spectra obtained on Mn(27)-Ce(7)-Zr and 1% Pd/Mn(27)-Ce(7)-Zr during NOx storage (Fig. S7) clearly shows that at 100 °C Pd promotes nitrite formation, i.e., favors NO adsorption and spillover, consistent with the low activity of Pd for NO oxidation at such low temperatures [45]. This, in turn, is beneficial for NOx release during subsequent temperature ramping, given the intrinsically lower thermal stability of nitrite compared to nitrate (Fig. S8).

The poor performance of 1.8% Pd/Mn(27)-Ce(7)-Zr after hydrothermal aging can be attributed to its decreased surface area and the loss of Pd due to encapsulation. Indeed, an increase in crystallinity of the support was observed for 1.8% Pd/Mn(27)-Ce(7)-Zr after aging, as indicated by growth of the primary crystallites and the detection of crystalline Mn_2O_3 and Mn_3O_4 in the aged 1.8% Pd/Mn(27)-Ce(7)-Zr sample. Likewise, sintering of MnO_x-CeO_2 mixed oxides after hydrothermal treatment has been reported by a number of authors [19,24,46-48].

Simulated cold start experiments confirmed the excellent properties of the 1.8%Pd/Mn(27)-Ce(7)-Zr catalyst with respect to NOx storage and release. Notably, reductants were found to interfere with the NOx storage, even though definite advantages from the presence of reductants were observed previously for a Pd/CZO catalyst [12] and Pd/zeolite catalysts [15,16]. This can be explained on the basis that the Mn in this formulation improves NOx storage by oxidizing the NO to NO_2, whereas reductants can reduce it back to NO. A similar interference has been observed previously for LNTs tested in the presence of hydrocarbons [49].

Hydrothermal aging of 1.8%Pd/Mn(27)-Ce(7)-Zr at 700 °C reduced the storage efficiency, although the catalyst was still able to store significant amounts of NOx. However, catalyst sulfation led to a large decrease in NOx storage efficiency. Unfortunately, catalyst desulfation is problematic, $MnSO_4$ in particular possessing high thermal stability. Indeed, according to the literature, thermal decomposition of $MnSO_4$ is not initiated until temperatures of 650-700 °C are reached, the exact value depending on the atmosphere (N_2 or air) and the heating rate [50-52]. Consequently, moderate thermal treatments cannot restore the original NOx storage capacity, while the use of more severe thermal treatments is precluded by the resulting thermal damage to the catalyst that would ensue.

5. Conclusions

Pd-promoted Mn-Ce(Pr)-Zr mixed oxides were found to show remarkable low temperature NOx storage efficiency in isothermal NO storage experiments. DRIFTS measurements showed that relative to Ce-Zr mixed oxides, Mn incorporation facilitated NOx storage as nitrate, in agreement with the high NO oxidation activity observed previously for MnO_x-CeO_2 mixed oxides. Consequently, NOx storage efficiency was found to improve with increase of the Mn content for the 1%Pd/Mn(x)-Ce(7)-Zr series (x = 9, 18, 27 wt.%). Similarly, a 1.8% Pd/Mn(27)-Ce(7)-Zr catalyst showed high levels of NOx storage in simulated cold start experiments. Ramping the temperature to 370 °C in these experiments resulted in near complete purging of stored NOx from the catalyst.

During TPD two main desorption events were observed, corresponding to decomposition of nitrites (up to 200 °C), followed by loss of nitrates (200 - 400 °C). As for MnO_x-CeO_2, nitrates formed on Pd/Mn-Ce(Pr)-Zr mixed oxides desorbed during TPD at lower temperatures than for

CeO_2-ZrO_2 mixed oxides, a finding that can be attributed to the lower basicity of Mn compared to Ce.

Hydrothermal aging of 1.8% Pd/Mn(27)-Ce(7)-Zr at 700 °C reduced the storage efficiency, although the catalyst was still able to store significant amounts of NOx. However, the presence of SO_2 led to a large decrease in NOx storage efficiency. Given the high thermal stability of $MnSO_4$, catalyst desulfation is problematic; indeed, moderate thermal treatments failed to restore the original NOx storage capacity, while the use of more severe thermal treatments is precluded by the resulting thermal damage to the catalyst that would ensue. Hence, it would be necessary to devise a rich regeneration protocol at a temperature sufficiently low to prevent thermal damage to the catalyst, which may not be practical, especially for diesel vehicles.

Acknowledgements

The authors thank Shelley Hopps for XRD measurements. This project was funded by the National Science Foundation and the U.S. Department of Energy (DOE) under award no. CBET-1258742. However, any opinions, findings, conclusions, or recommendations expressed herein are those of the authors and do not necessarily reflect the views of the DOE.

References

[1] F. Millo, D. Vezza, SAE Technical Paper 2012-01-0373.

[2] J. Theis, C. Lambert, Catal. Today 258 (2015) 367-377.

[3] J. Cole, U.S. Patent 5,656,244, August 12, 1997.

[4] M. Jarvis, K. Adams, U.S. patent 6,182,443, February 6, 2001.

[5] J. Melville, R. Brisley, O. Keane, P. Phillips, U.S. Patent No. 8,105,559 B2, January 31, 2012.

[6] H. Chen, S. Mulla, U.S. Patent Pub. No. 2012/0308439 A1, December 6, 2012.

[7] H. Chen, S. Mulla, E. Weigert, K. Camm, T. Ballinger, J. Cox, P. Blakeman, SAE Technical Paper 2013-01-0535.

[8] Y. Murata, T. Morita, K. Wada, H. Ohno, SAE Technical Paper 2015-01-1002.

[9] S. Jones, Y. Ji, M. Crocker, Catal. Lett., 146 (2016) 909-917.

[10] S. Jones, Y. Ji, A. Bueno-Lopez, V. Song, M, Crocker, Emission Control Sci. Technol., 3 (2017) 59-72.

[11] Y. Ji, D. Xu, S. Bai, U. Graham, M. Crocker, B. Chen, C. Shi, D. Harris, D. Scapens, J. Darab, Ind. Eng. Chem. Res. 56(1) (2017) 111-125.

[12] J. Theis, Catal. Today 267 (2016) 93-109.

[13] Y. Ryou, J. Lee, H. Lee, C.H. Kim, D.H. Kim, Catal. Today, 2017, 307 (2018) 93-101.

[14] H. Chen, J.E. Collier, D. Liu, L. Mantarosie, D. Durán-Martín, V. Novák, R.R. Rajaram, D. Thompsett, Catal. Lett., 146 (2016) 1706-1711.

[15] A. Vu, J. Luo, J. Li, W.S. Epling, Catal. Lett., 147 (2017) 745-750.

[16] Y. Zheng, L. Kovarik, M.H. Engelhard, Y. Wang, Y. Wang, F. Gao, J. Szanyi, J. Phys. Chem. C, 121 (2017) 15793-15803.

[17] Y. Ryou, J. Lee, S.J. Cho, H. Lee, C.H. Kim, D.H. Kim, Appl. Catal. B, 212 (2017) 140-149.

[18] W. Wang, G. McCool, N. Kapur, G. Yuan, B. Shan, M. Nguyen, U. Graham, B. Davis, G. Jacobs, K. Cho, X. Hao, Science, 337 (2012) 832-835.

[19] G. Qi, W. Li, Catal. Today, 258 (2015) 205-213.

[20] Z. Zhang, B. Chen, X. Wang, L. Xu, C. Au, C. Shi, M. Crocker, Appl. Catal. B, 165 (2015) 232-244.

[21] N. Le Phuc, X. Courtois, F. Can, S. Royer, P. Marecot, D. Duprez, Appl. Catal. B, 102 (2011) 362-371.

[22] J.H. Xiao, X.H. Li, S. Deng, F.R. Wang, L.F. Wang, Catal. Commun., 9 (2008) 563-567.

[23] H. Huang, R.T. Yang, Langmuir, 17 (2001) 4997-5003.

[24] M. Machida, M. Uto, D. Kurogi, T. Kijima, Chem. Mater., 12 (2000) 3158-3164.

[25] M. Machida, Catal. Surv. Jpn., 5 (2002) 91-102.

[26] L. Guo, H. Xian, Q. Li, D. Chen, Y. Tan, J. Zhang, L. Zheng, X. Li, J. Hazard. Mater., 260 (2013) 543-551.

[27] L. Guo, L. Guo, D. Zhao, Z. Gao, Y. Tian, T. Ding, J. Zhang, L. Zheng, X. Li, Catal. Today, 297 (2017) 27-35.

[28] L. Xueting, L. Shujun, H. Hui, W. Zeng, W. Junliang, C. Limin, Y. Daiqi, F. Mingli, Appl. Catal. B, 223 (2018) 91-102.

[29] J.I. Gutiérrez-Ortiz, B. de Rivas, R. López-Fonseca, S. Martín, J.R. González-Velasco, Chemosphere, 68 (2007) 1004-1012.

[30] V.R. Galakhov, M. Demeter, S. Bartkowski, M. Neumann, N.A. Ovechkina, E.Z. Kurmaev, N.I. Lobachevskaya, Ya. M. Mukovskii, J. Mitchell, D.L. Ederer, Phys. Rev. B, 65 (2002) 113102/1-113102/4.

[31] I. Barrio, I. Legórburu, M. Montes, M.I. Dominguez, M.A. Centeno, J.A. Odriozola, Catal. Lett., 101 (2005) 151-157.

[32] NIST X-ray Photoelectron Spectroscopy Database, Version 4.1, 2012, https://srdata.nist.gov/xps/.

[33] X. Wu, Q. Liang, D. Weng, J. Rare Earths, 24 (2006) 549-553.

[34] F. Buciuman, F. Patcas, R. Cracium, D.R.T. Zahn, Phys. Chem. Chem. Phys., 1 (1999) 185-190.

[35] I. Atribak, B. Azambre, A. Bueno López, A. García-García, Appl. Catal B, 92 (2009) 126-137.

[36] C. Binet, M. Daturi, J.-C. Lavalley, Catal. Today, 50 (1999) 207-225.

[37] K. Hadjiivanov, Cat. Rev.-Sci. Eng., 42 (2000) 71-144.

[38] S. Philipp, A. Drochner, J. Kunert, H. Vogel, J. Theis, E. Lox, Top. Catal. 30 (2004) 235-238.

[39] M. Kantcheva, J. Catal., 204 (2001) 479-494.

[40] R. Fricke, E. Schreier, R. Eckelt, M. Richter, A. Trunschke, Top. Catal., 30 (2004) 193-198.

[41] G. Qi and R.T. Yang, J. Phys. Chem. B, 108 (2004) 15738-15747.

[42] W.S. Epling, L.E. Campbell, A. Yezerets, N.W. Currier, J.E. Parks II, Catal. Rev., 46(2) (2004) 163-245.

[43] H. Chen, A. Sayari, A. Adnot, F. Larachi, Appl. Catal. B 32 (2001) 195-204.

[44] S. Imamura, A. Doi, S. Ishida, Ind. Eng. Chem. Prod. Res. Dev., 24 (1985) 75-80.

[45] X. Auvray, L. Olsson, 168-169 (2015) 342-352.

[46] B. Murugan and A.V. Ramaswamy, Chem. Mater., 17 (2005) 3983-3993.

[47] Q. Liang, X. Wu, D. Weng, H. Xu, Catal. Today, 139 (2008) 113-118.

[48] W. Shan, M. Luo, P. Ying, W. Shen, C. Li, Appl. Catal. A 246 (2003) 1-9.

[49] S. Katare, J. Patterson, P. Laing, Society of Automotive Engineers Technical Paper 2007-01-3984, 2007.

[50] H. Tagawa, Thermochimica Acta, 80 (1984) 23-33.

[51] J. Mu and D. Perlmutter, Ind. Eng. Chem. Process Des. Dev., 20 (1981) 640-646.

[52] J.P. McWilliams and A.N. Hixson, Ind. Eng. Chem. Process Des. Dev., 15 (1976) 365-371.

Figure captions

Fig. 1. Powder X-ray diffraction patterns of the samples

Fig. 2. H_2-TPR profiles of the samples

Fig. 3. NOx storage and desorption efficiency as a function of adsorption temperature over Mn(27)-Ce(7)-Zr and 1.0% Pd/Mn(27)-Ce(7)-Zr

Fig. 4. NOx storage efficiency at 120 °C and desorption behavior during NOx-TPD for mixed oxides promoted with 1.0% Pd

Fig. 5. Comparison of NOx storage and desorption efficiency before and after aging for mixed oxides promoted with 1.0% Pd

Fig. 6. DRIFT spectra collected during NOx storage at 100 ºC on Pd-promoted Mn(27)-Ce(7)-Zr

Fig. 7. DRIFT spectra collected during NOx-TPD from Pd-promoted Mn(27)-Ce(7)-Zr

Fig. 8. DRIFT spectra for 1.0% Pd/Mn(10)-Pr(10)-Zr collected during NOx storage at 100 °C and subsequent NOx-TPD

Fig. 9. NOx slip for degreened 1.8% Pd/Mn(27)-Ce(7)-Zr formulation during initial 800 s of lean transient tests with 110 ppm NO, 5% H_2O, 5% CO_2, 10% O_2, and balance N_2. Sample evaluated without reductant, with 250 ppm C_2H_4, and with 1350 ppm CO + 450 ppm H_2.

Fig. 10. Cumulative NOx stored for degreened 1.8% Pd/Mn(27)-Ce(7)-Zr formulation during lean transient tests with 110 ppm NO, 5% H_2O, 5% CO_2, 10% O_2, and balance N_2. Sample evaluated without reductant, with 250 ppm C_2H_4, and with 1350 ppm CO + 450 ppm H_2.

Fig. 11. NOx slip during initial 800 s of lean transient tests for 1.8% Pd/Mn(27)-Ce(7)-Zr formulation with 110 ppm NO, 5% H_2O, 5% CO_2, 10% O_2, and balance N_2. Sample evaluated on one test after degreening at 500 ºC and on two tests after aging 15 h at 700 ºC in a lean mixture.

Fig. 12. NOx slip during initial 800 s of lean transient tests for 1.8% Pd/Mn(27)-Ce(7)-Zr formulation with 110 ppm NO, 5% H_2O, 5% CO_2, 10% O_2, and balance N_2. Sample evaluated on one test after degreening at 500 ºC, on two tests after 15 h at 700 ºC, and on one test after an additional 15 h at 350 ºC with 5 ppm SO_2, 5% H_2O, 5% CO_2, 10% O_2, and balance N_2.

Fig. 13. NOx slip during initial 800 s of lean transient tests for 1.8% Pd/Mn(27)-Ce(7)-Zr formulation with 110 ppm NO, 5% H_2O, 5% CO_2, 10% O_2, and balance N_2. Sample evaluated on one test after 15 h at 700 ºC, on one test after an additional 15 h at 350 ºC with 5 ppm SO_2, and on tests following 15 min lean desulfations at 760 ºC, 790 ºC, and 815 ºC.

Fig. 1

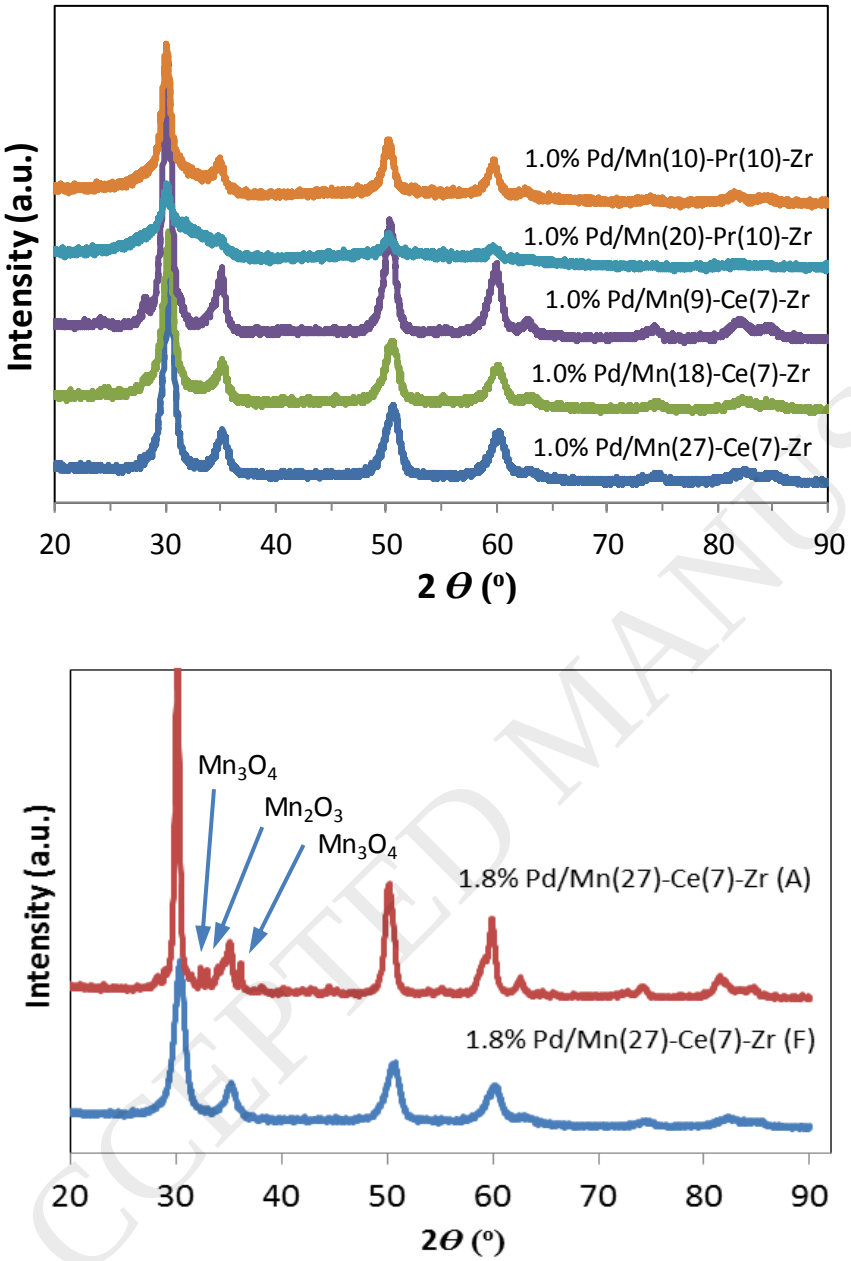

Fig. 2

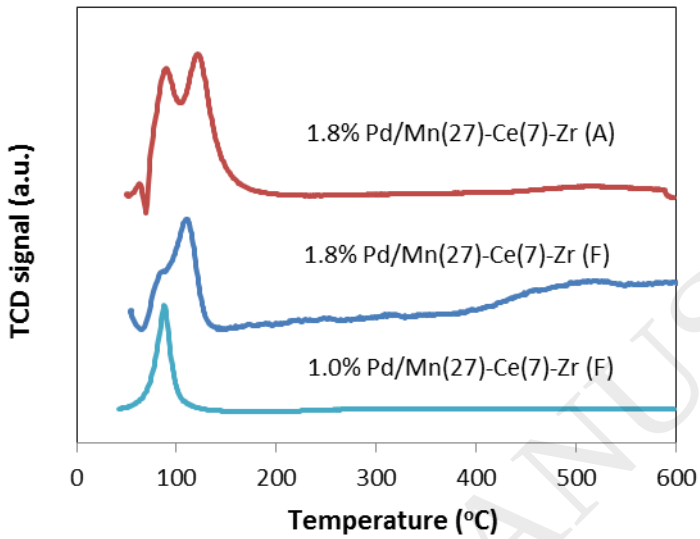

Fig. 3

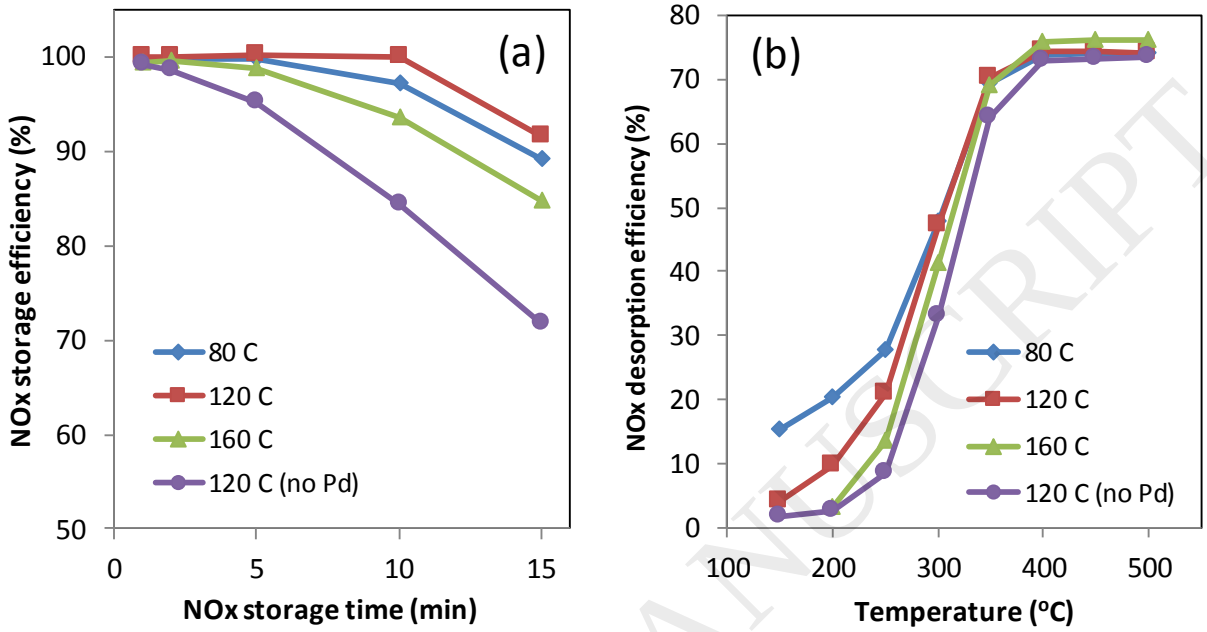

Fig. 4

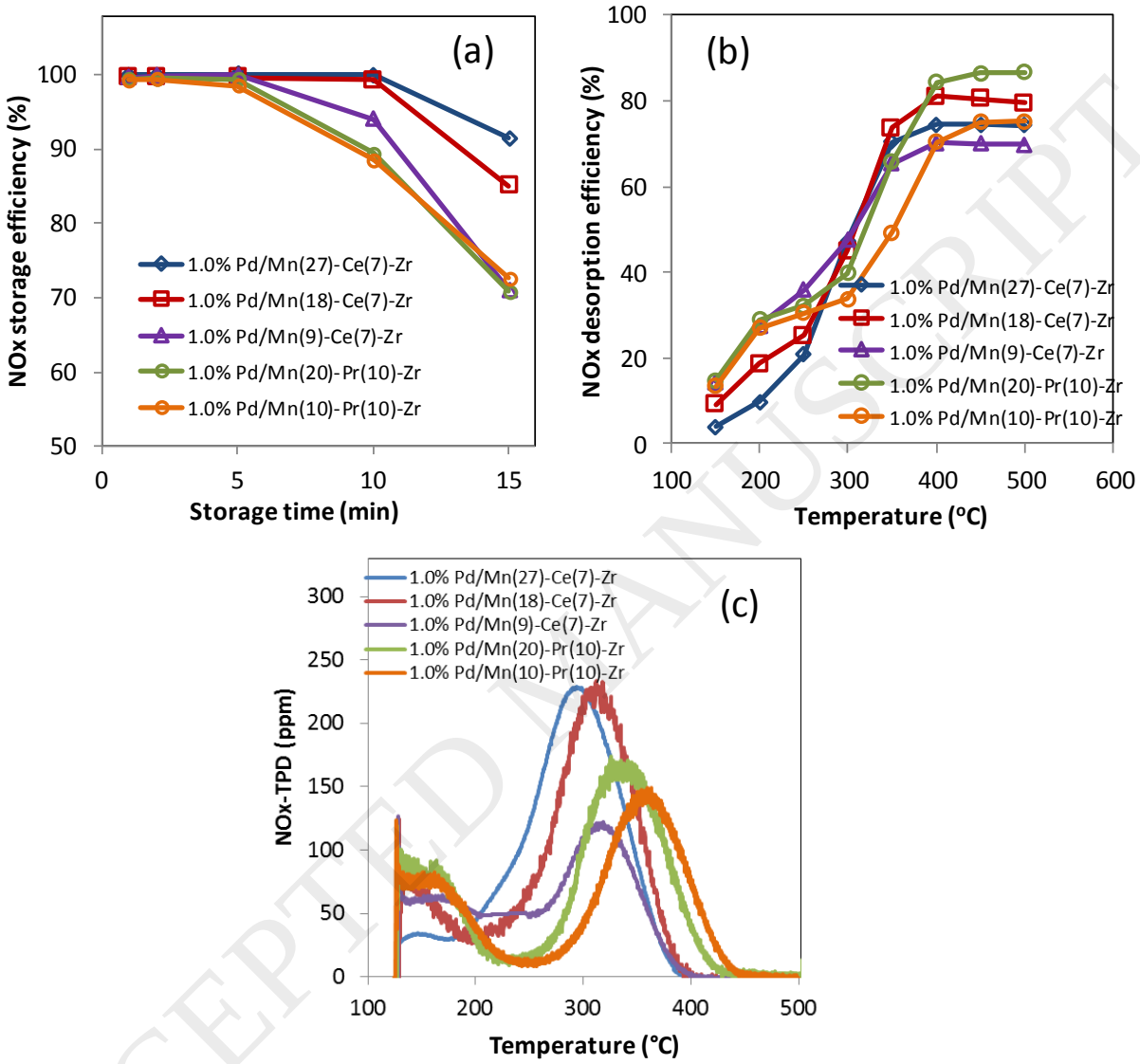

Fig. 5

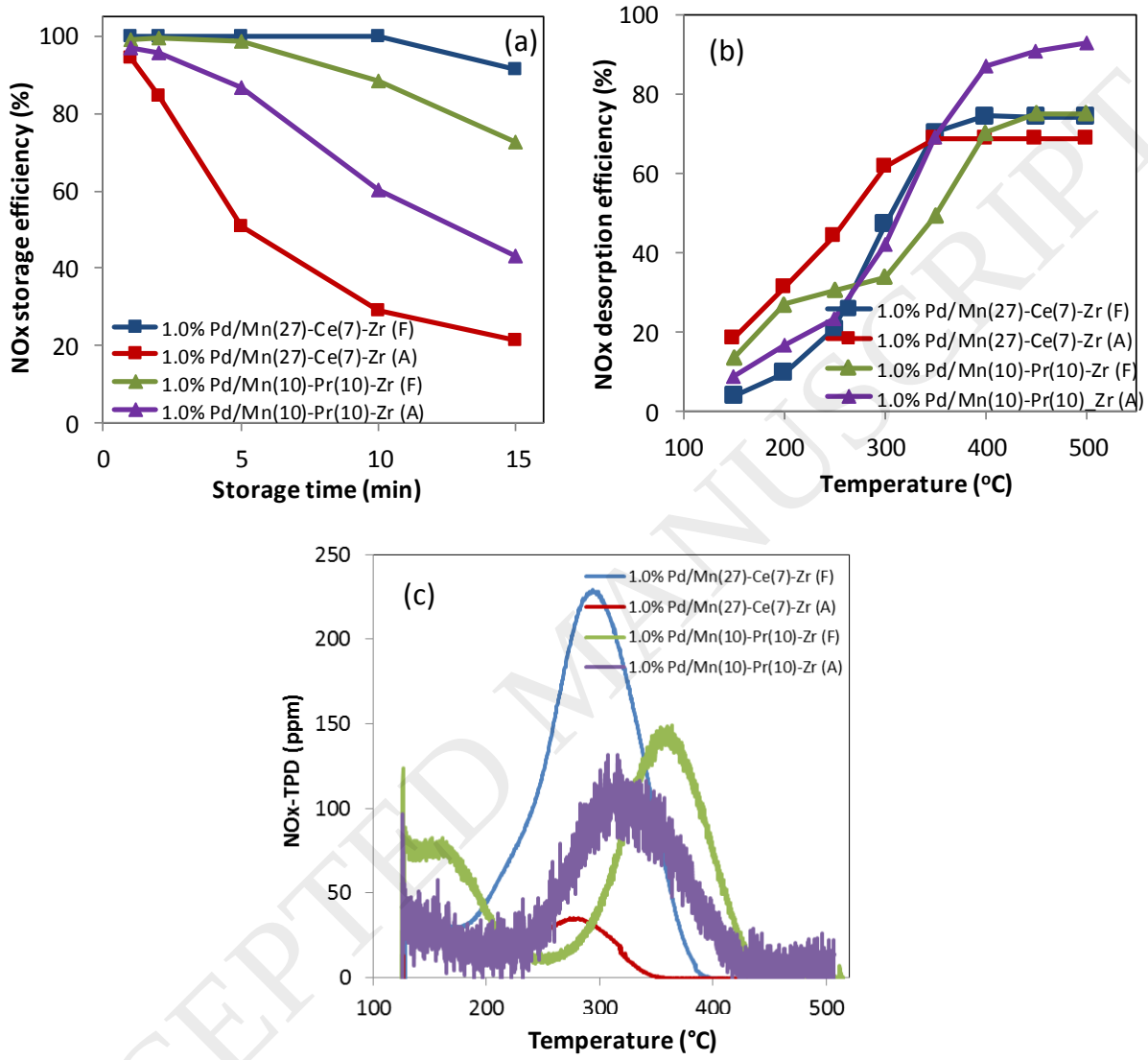

Fig. 6

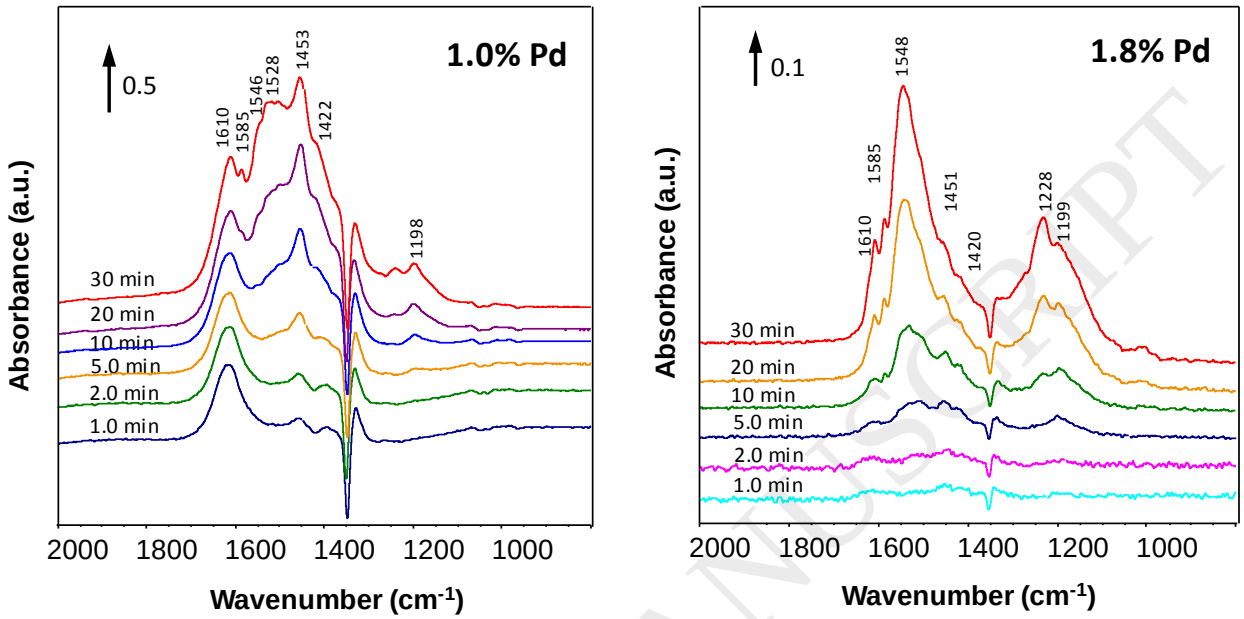

Fig. 7

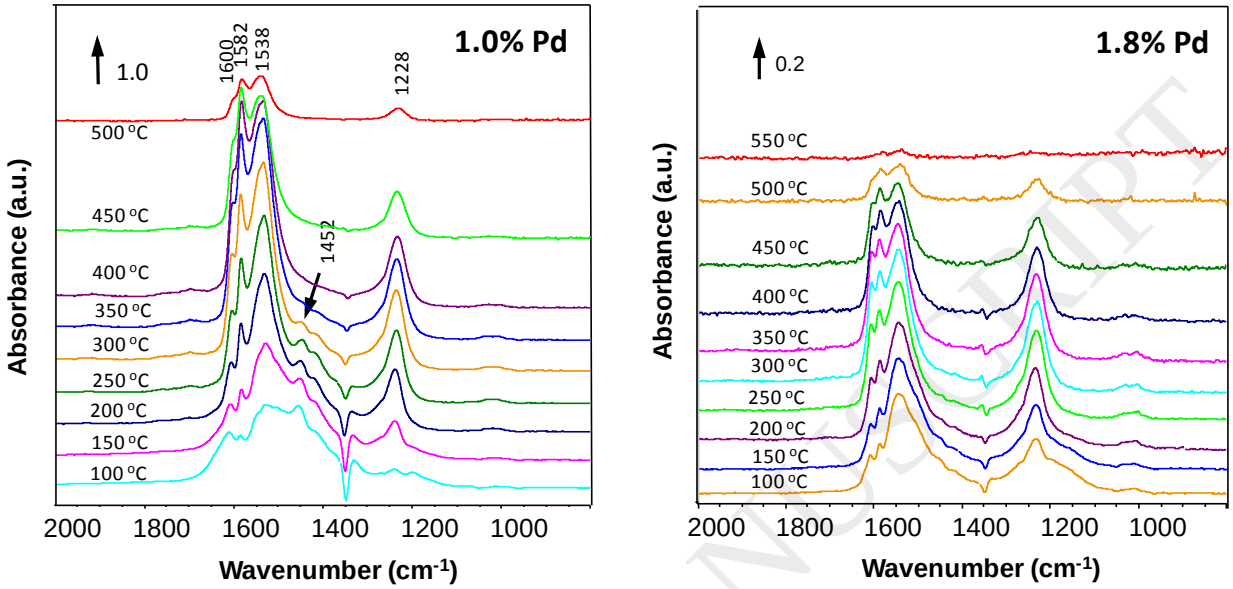

Fig. 8

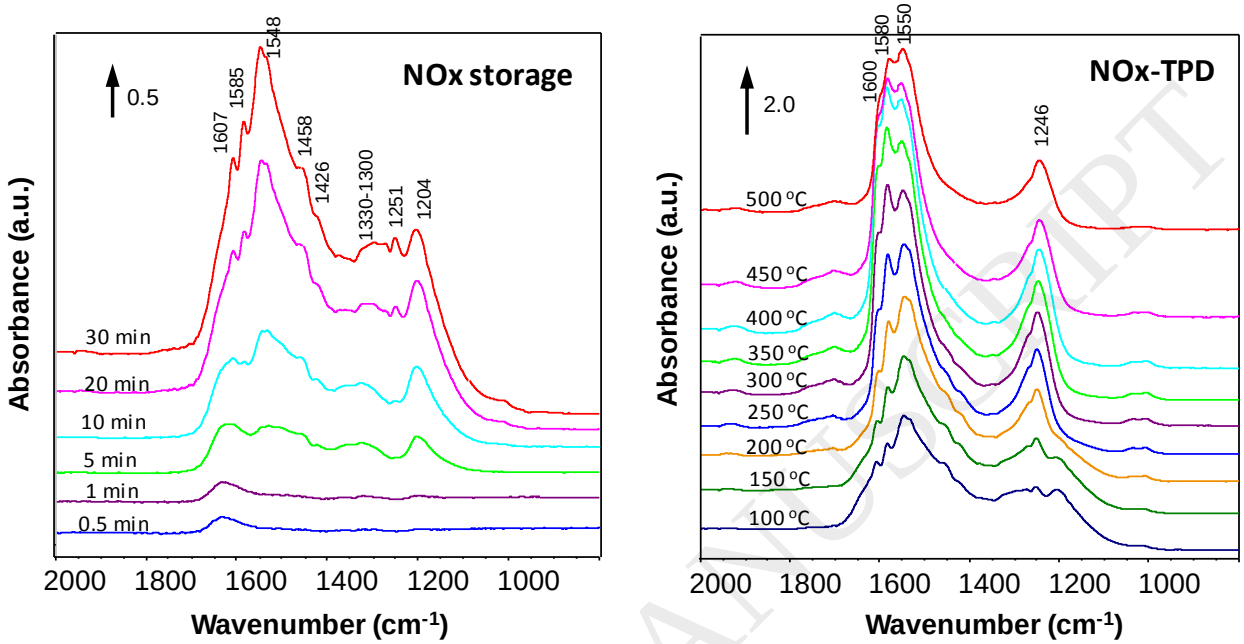

Fig. 9

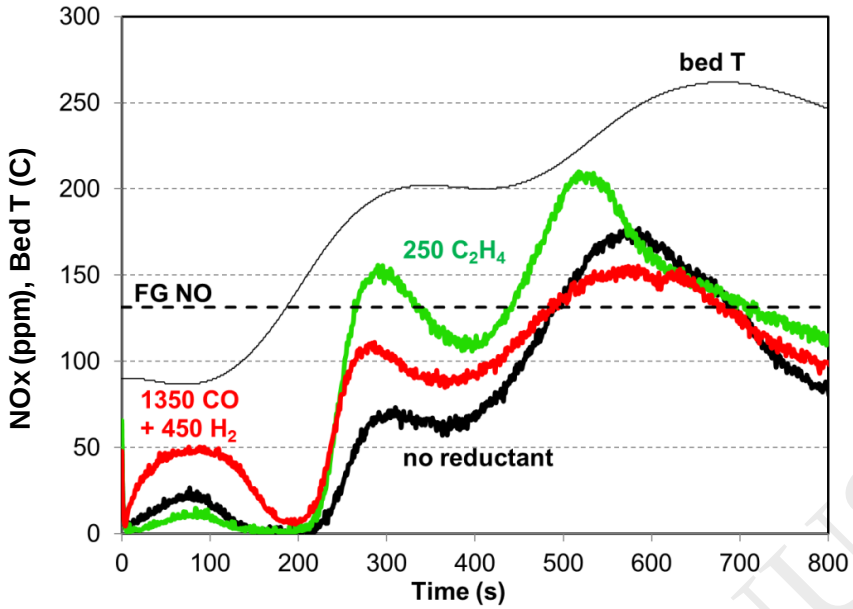

Fig. 10

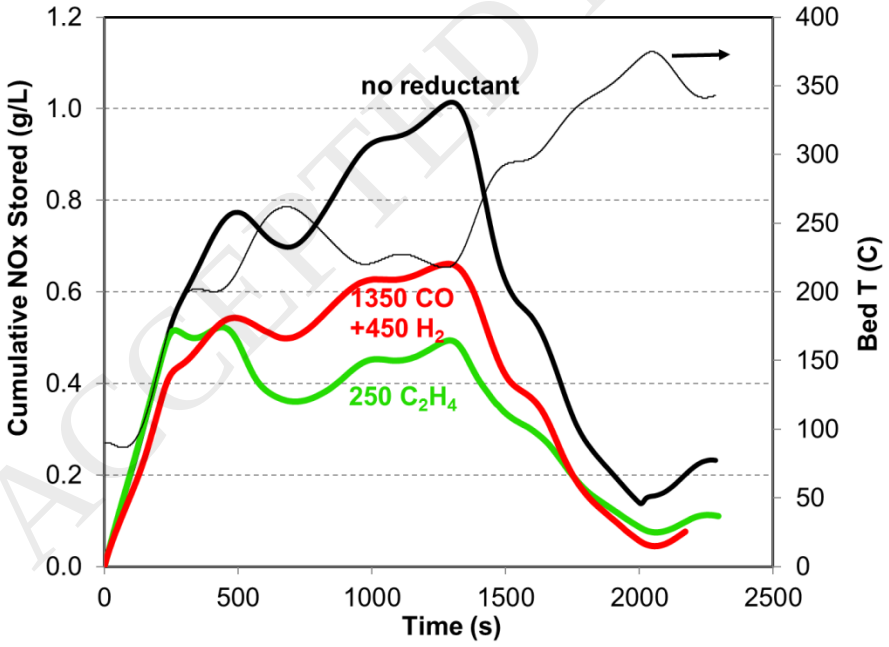

Fig. 11

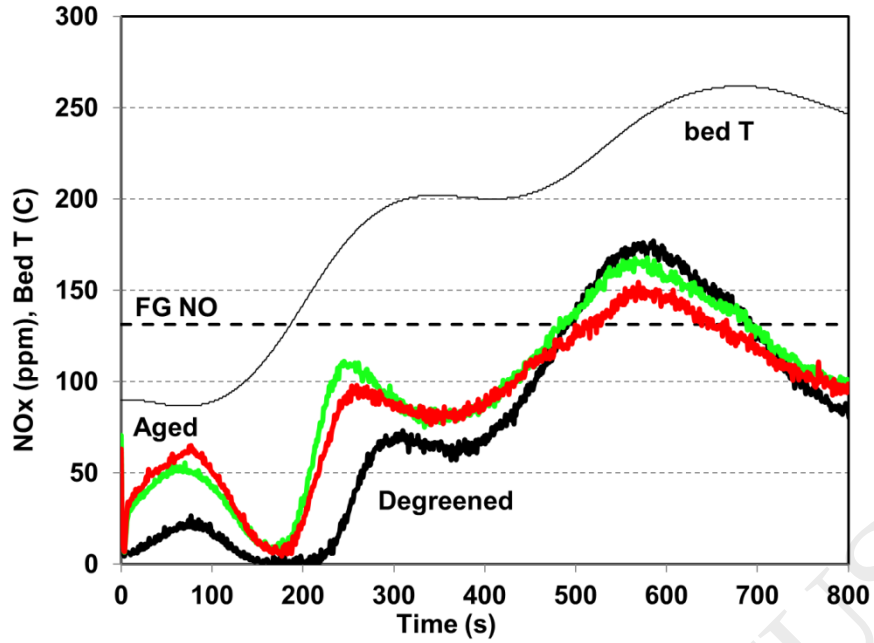

Fig. 12

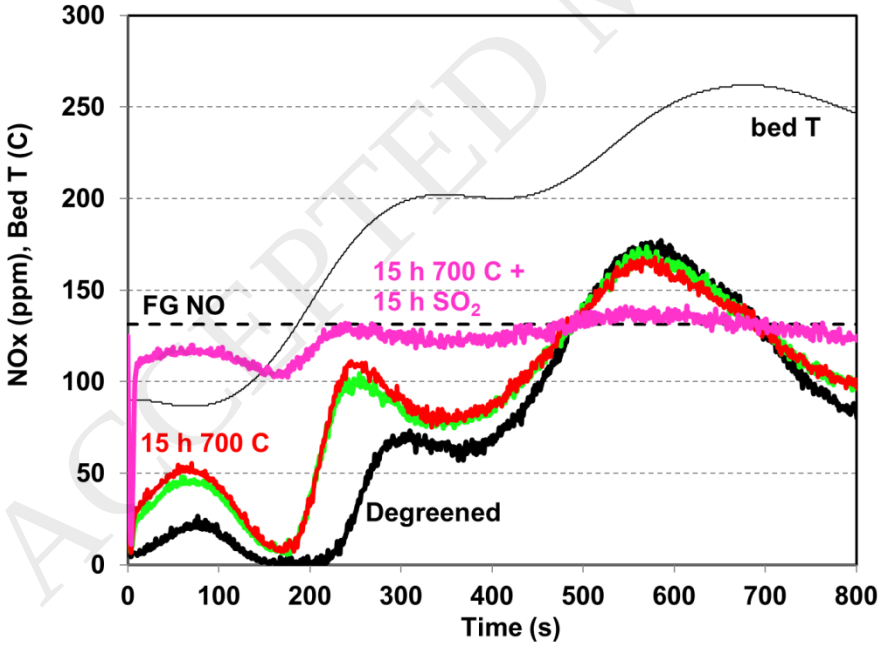

Fig. 13

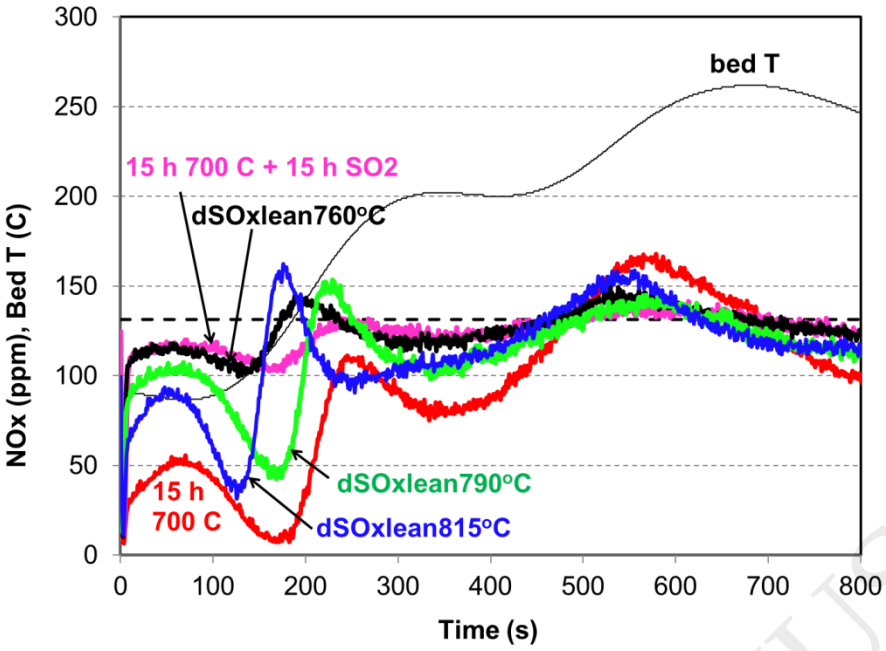

Table 1. Physical properties of Mn-based mixed oxides used in this work

Sample[a]	BET SA (m^2/g)	Pore Vol. (cm^3/g)	Av. Pore Radius (nm)	Mean Pd Particle Size (nm)	Crystal Size (mn)
1.0% Pd/Mn(27)-Ce(7)-Zr (F)	112	0.37	6.64	6.67	8.04
1.0% Pd/Mn(18)-Ce(7)-Zr (F)	129	0.41	6.41	9.84	8.17
1.0% Pd/Mn(9)-Ce(7)-Zr (F)	78	0.37	9.19	8.09	9.89
1.0% Pd/Mn(20)-Pr(10)-Zr (F)	142	0.42	5.86	7.59	-[b]
1.0% Pd/Mn(10)-Pr(10)-Zr (F)	130	0.41	6.25	4.34	9.53
1.8% Pd/Mn(27)-Ce(7)-Zr (F)	101	0.33	6.60	8.18	7.79
1.8% Pd/Mn(27)-Ce(7)-Zr (A)	20.7	0.10	9.59	27.35	17.14

[a] F= fresh; A = hydrothermally aged (750 °C, 16 h). [b] Accurate determination hampered by the presence of monoclinic and tetragonal phases, resulting in broad diffraction peaks.